ChemPhysMater 5 (2026) 493–503

Contents lists available at ScienceDirect

ChemPhysMater

journal homepage: https://www.keaipublishing.com/en/journals/chemphysmater/

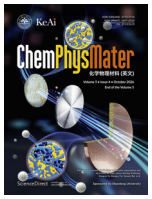

Research Article

Controllable synthesis of trisoctahedral Au@Pd core-shell nanoparticles with tunable Pd shell thickness for enhanced ethanol electrooxidation

Li Kong

State Key Laboratory of Crystal Materials, Institute of Crystal Materials, Shandong University, Jinan 250100, China

ARTICLE INFO

Keywords:
Au@Pd
Core-shell nanoparticles
Pd shell thickness
High index facet
Electrocatalysis

ABSTRACT

Efficient palladium-based electrocatalysts are crucial for ethanol oxidation in fuel cells. Here, a series of TOH-Au@Pd$_x$ core-shell nanoparticles with precisely controlled Pd shell thicknesses were successfully synthesized using well-defined trisoctahedral Au seeds (~45 nm). The prepared nanoparticles are uniform, and the Pd shell thickness progressively grows from 0.54 to 1.39 nm. XPS analysis reveals significant electronic interactions between the Au core and Pd shell, with the binding energy shifts of the Au 4f and Pd 3d core levels systematically decreasing as the shell thickness increases. All TOH-Au@Pd$_x$ catalysts surpass commercial Pd/C, with TOH-Au@Pd$_{40}$ showing the highest activity: an electrochemical surface area of 128.8 m^2/g, a mass activity of 13.6 A/mg, and a specific activity of 10.6 mA/cm^2, corresponding to 5.0-, 68.0-, and 13.3-fold improvements over Pd/C. It also exhibits the smallest Tafel slope and charge transfer resistance, indicating the most favorable reaction kinetics and interfacial charge transfer capability. Moreover, it retains 27.5% of its initial current after 7200 s, far exceeding Pd/C (1.4%). The enhanced performance arises from the synergy between the high-index facets (rich in steps, edges, and kinks) of the trisoctahedral morphology and the optimal electronic interaction between the Au core and the Pd shell. This study not only provides an effective strategy for the controlled synthesis of high-performance core-shell catalysts but also offers fundamental insights into how geometric and electronic effects jointly govern electrocatalytic activity and stability.

1. Introduction

Direct ethanol fuel cells (DEFCs) have garnered significant interest as a promising clean energy technology due to the wide availability, high energy density, and safe handling of ethanol [1–3]. However, their commercialization faces major obstacles such as sluggish ethanol oxidation reaction (EOR) kinetics, high cost of noble metal catalysts, and catalyst poisoning by reaction intermediates [4,5]. In alkaline media, Pd-based catalysts exhibit higher initial activity and better selectivity for EOR than Pt-based ones [6,7]. However, pure Pd nanocatalysts still suffer from limited active sites, gradual deactivation due to intermediate adsorption during prolonged operation, and low noble metal utilization efficiency [8,9]. Thus, developing Pd-based catalysts that combine high activity, stability, and atomic economy remains a key research priority.

To address these challenges, the construction of core-shell nanostructured catalysts has emerged as a promising strategy [10,11]. In particular, the Au@Pd system—consisting of a gold (Au) core and a palladium (Pd) shell—has attracted considerable interest [12–15]. This architecture combines the distinct advantages of both metals: the Au core provides high chemical stability and electrical conductivity, while its closely matched lattice parameters with Pd facilitate epitaxial shell growth, minimizing lattice-mismatch strain and ensuring structural integrity of the heterostructure [16,17]. Moreover, the pronounced electronic interaction between Au and Pd effectively tunes the electronic structure of surface Pd atoms. Both theoretical and experimental evidence indicates a partial electron transfer from the Pd shell to the Au core, resulting in a downshift of the Pd d-band center [18,19]. Such electronic modulation optimizes the adsorption behavior of oxygen-containing intermediates on Pd, thereby enhancing intrinsic activity while improving poisoning resistance [20]. Additionally, the core-shell design maximizes the exposure of catalytically active Pd atoms at the surface, leading to significantly improved mass activity and contributing to more economical use of precious metals [18].

In recent years, Au@Pd catalysts with diverse morphologies, including spherical [21], cubic [22], and octahedral nanostructures [23], have been successfully synthesized. These catalysts generally exhibit superior ethanol oxidation performance compared to conventional Pd/C. Such studies have laid a preliminary foundation for understanding the correlations between catalyst morphology, size, and electrochemical performance. Nevertheless, current research remains largely focused on regular polyhedra that predominantly expose low-index crystal facets. In contrast, high-index-faceted nanostructures—which possess surfaces rich in catalytically active sites such as steps, edges, and kinks—have received considerably less attention [24–26]. Owing to their high den-

E-mail address: kongli@sdu.edu.cn

https://doi.org/10.1016/j.chphma.2026.04.002
Received 24 January 2026; Received in revised form 8 April 2026; Accepted 27 April 2026
Available online 30 April 2026
2772-5715/© 2026 The Authors. Publishing Services by Elsevier B.V. on behalf of KeAi Communications Co. Ltd. This is an open access article under the CC BY-NC-ND license (http://creativecommons.org/licenses/by-nc-nd/4.0/)

sity of undercoordinated atoms, such high-index facets generally exhibit substantially enhanced intrinsic activity [27,28]. Therefore, systematic exploration of these structures is essential to advance the fundamental understanding and further optimize the catalytic performance of Au@Pd systems.

Based on the above analysis, well-defined trisoctahedral gold nanoparticles (TOH-Au NPs) with high-index-faceted surfaces were selected as structural templates in this work. Through precise control of the Na_2PdCl_4 precursor amount, tunable Pd shell deposition was achieved, successfully yielding a series of core-shell TOH-Au@Pd_x nanoparticles with continuously adjustable shell thickness. Systematic electrochemical tests demonstrated that all catalysts in this series exhibit enhanced activity and stability for ethanol electro-oxidation compared to commercial Pd/C, with TOH-Au@Pd_{40} showing the most pronounced performance. This study not only offers a viable strategy for the rational design and controllable synthesis of high-performance core-shell catalysts, but also establishes experimental and theoretical foundations for the development of practical fuel cell catalysts from the perspective of synergistic modulation of geometric structure and electronic effects.

2. Experimental section

2.1. Materials and apparatus

L-ascorbic acid (AA, 99%), hydrogen tetrachloroaurate tetrahydrate ($HAuCl_4{\cdot}4H_2O$, 99%), sodium borohydride ($NaBH_4$, 99%), and cetyltrimethylammonium chloride (CTAC, 99%) were purchased from Sinopharm Chemical Reagent Co., Ltd. Sodium tetrachloropalladate(II) hydrate (Na_2PdCl_4, 99%), commercial Pd/C catalysts (nominally 10% on carbon black) were purchased from Alfa Aesar (Shanghai, China). These reagents were used as received without further purification. All glassware was cleaned with aqua regia solution and subsequently rinsed three times with deionized water prior to use. Milli-Q water with a resistivity of 18.2 MΩ cm was employed for all experimental procedures. Caution: Aqua regia is highly corrosive and must be handled with extreme care; it should never be stored in sealed containers.

Transmission electron microscopy (TEM) characterization was performed on a JEOL JEM-2100F instrument operated at 200 kV. The average nanoparticle size was estimated based on statistical analysis of approximately 200 individual particles from the TEM images. High-angle annular dark-field scanning transmission electron microscopy (HAADF-STEM) imaging and corresponding energy-dispersive X-ray spectroscopy (STEM-EDS) elemental mapping were conducted using the same microscope equipped with a STEM unit. X-ray photoelectron spectroscopy (XPS) measurements were carried out on an ESCALAB 250 system with a monochromatic Al Kα X-ray source ($h\nu$ = 1486.6 eV). X-ray diffraction (XRD) patterns were recorded on a Rigaku Miniflex 600 diffractometer employing Cu Kα radiation and a graphite monochromator, with data collected over a 2θ range of 30°–90° at a step size of 0.02°.

2.2. Synthesis of TOH-Au@Pd_x NPs

The 45 nm TOH-Au nanoparticles employed in this work were synthesized following a method previously reported by our group [29]. The preparation of TOH-Au@Pd_x nanoparticles was carried out as follows: into a small reaction vial, 1.9 mL of 0.05 mol/L CTAC solution was introduced, followed by the addition of pre-synthesized TOH-Au nanoparticles as seeds. Under continuous stirring, 10 μL of 1 mol/L HCl, 40 μL of 2 mmol/L Na_2PdCl_4 solution, and 40 μL of 4 mmol/L ascorbic acid (AA) solution were added sequentially. The mixture was allowed to react under stirring at room temperature for 3 h. The resulting TOH-Au@Pd_{40} nanoparticles were then separated from the growth solution by centrifugation at 9600 r/min for 5 min and washed three times with Milli-Q water. It is noteworthy that, for samples with varying Pd shell thicknesses, the volume of Na_2PdCl_4 was adjusted according to the experimental design, while the volume of AA was always maintained equal to that of Na_2PdCl_4 to ensure stoichiometric control during reduction.

For comparative analysis, pure Pd nanoparticles (Pd NPs) used in XPS characterization were prepared following an identical procedure, except that no TOH-Au seeds were introduced.

2.3. Electrochemical measurements

Electrochemical measurements were conducted on a CHI601E electrochemical workstation with a standard three-electrode configuration at room temperature. An Ag/AgCl electrode served as the reference, a platinum wire as the counter electrode, and a polished 3 mm diameter glassy carbon electrode (GCE) as the working electrode. The as-prepared TOH-Au@Pd_x NPs were collected by centrifugation, washed thoroughly, and redispersed in 150 μL of deionized water. Subsequently, 5 μL of the resulting suspension was drop-cast onto the GCE surface and dried under ambient conditions. Finally, the modified electrode was covered with 10 μL of 0.2 wt% Nafion aqueous solution and dried again at room temperature to form a stable catalyst layer.

Electrochemical ethanol oxidation was performed in a 0.50 mol/L KOH solution containing 0.5 mol/L ethanol. Electrochemical impedance spectroscopy (EIS) measurements were performed over a frequency range of 100 kHz to 0.1 Hz with an AC amplitude of 5 mV. Chronoamperometric measurements were carried out at a fixed potential of −0.3 V (vs. Ag/AgCl). All electrolyte solutions were deaerated by purging with high-purity nitrogen (99.99%) for 30 min prior to each experiment to remove dissolved oxygen.

All measurements were repeated three times to ensure reproducibility.

3. Results and discussion

3.1. Synthesis and characterization of TOH-Au@Pd_x NPs

TOH-Au NPs with a size of 45 nm and enclosed by high-index {331} facets were previously synthesized by our group (Fig. S1), and their catalytic activity toward methanol oxidation was evaluated [29]. Such high-index facets are known to provide surfaces rich in active sites—including steps, edges, and kinks—which contribute to their enhanced catalytic performance [30,31].

In the present work, using these 45 nm TOH-Au nanoparticles as seeds, a series of core-shell TOH-Au@Pd_x nanoparticles were synthesized by controlled addition of the precursor Na_2PdCl_4. As revealed by low magnification transmission electron microscopy (TEM) images (Figs. 1(a)(c)(e)(g)(i)(k)(m)), all obtained nanoparticles maintain a well-defined trisoctahedral morphology, exhibit high monodispersity, and show no significant aggregation.

A systematic statistical analysis of nanoparticle sizes was performed based on the low-magnification TEM images (Figs. 1(a)(c)(e)(g)(i)(k)(m)). The results indicate a clear correlation between the volume of Na_2PdCl_4 solution added and the resulting particle size. As the added volume was gradually increased from 15 to 30, 40, 50, 60, 80, and 120 μL, the mean particle diameter—determined from measurements of over 200 individual nanoparticles for each condition—rose correspondingly from 46.81 to 47.13, 47.20, 47.46, 47.89, 48.15, and 48.27 nm (Table 1). This monotonic and controlled increase in size with increasing precursor addition confirms the successful and uniform deposition of a Pd shell onto the Au core surface. Moreover, all samples exhibited a relative standard deviation (RSD) in particle size below 5%, underscoring the high size uniformity of the synthesized nanoparticles.

The microstructure of the nanoparticles was characterized in detail by high-resolution transmission electron microscopy (HRTEM), with the results shown in Figs. 1(b)(d)(f)(h)(j)(l)(n). A distinct core-shell architecture is clearly observed, consisting of a darker-contrast core and a

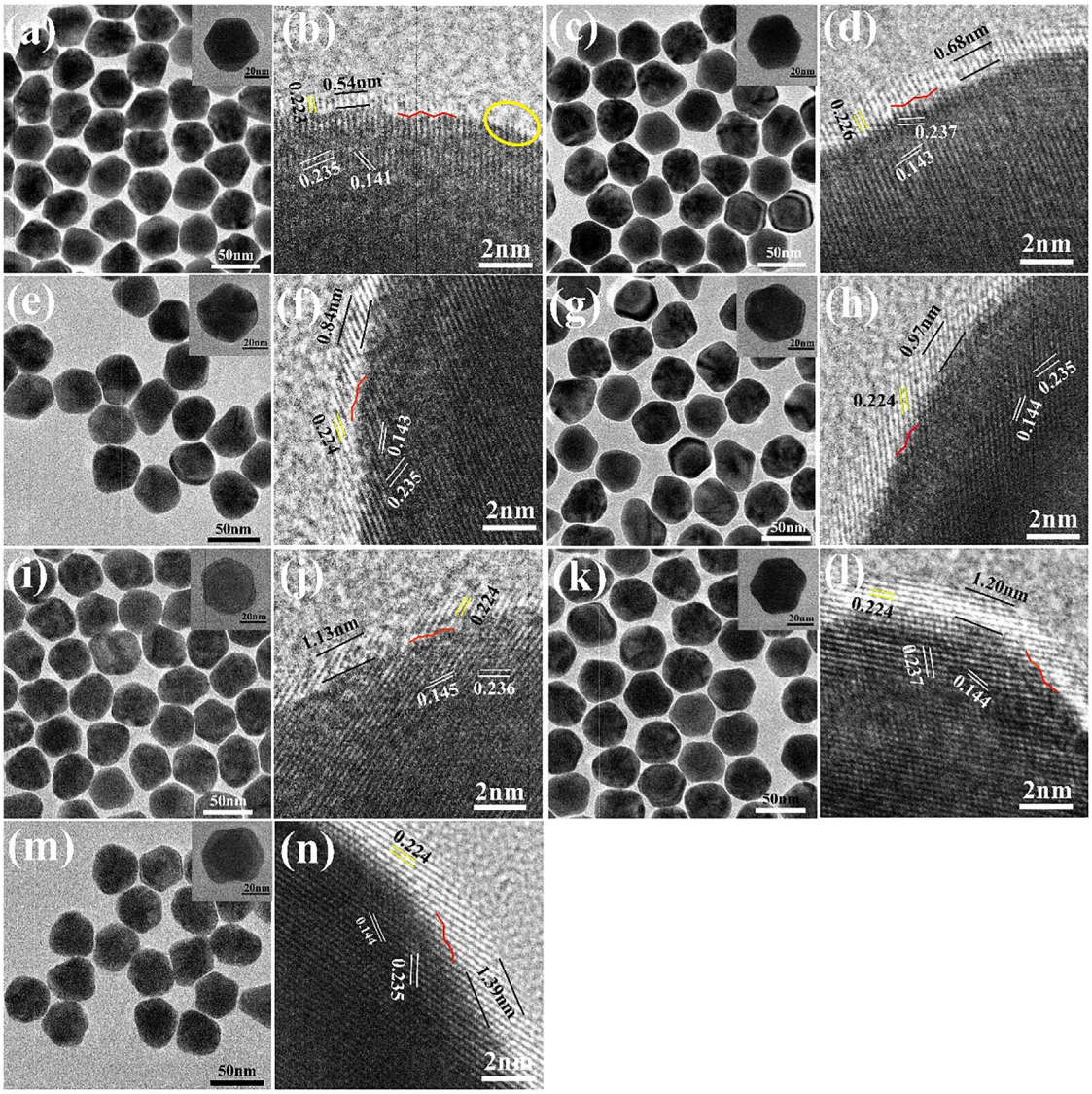

Fig. 1. Low magnification and their corresponding high-resolution TEM images of TOH-Au@Pd_x NPs obtained using different amounts of Na_2PdCl_4. (a)(b) 15 μL; (c)(d) 30 μL; (e)(f) 40 μL; (g)(h) 50 μL; (i)(j) 60 μL; (k)(l) 80 μL; (m)(n) 120 μL. The inset in low magnification images displays a representative individual nanoparticle.

Table 1
Summarized data of TOH-Au@Pd_x NPs.

Sample	Particle size (nm)	Relative Standard Deviation, RSD (%)	Shell thickness (nm)
TOH-Au@Pd_{15}	46.81	4.05	0.54 ± 0.05
TOH-Au@Pd_{30}	47.13	3.37	0.68 ± 0.04
TOH-Au@Pd_{40}	47.20	4.57	0.84 ± 0.04
TOH-Au@Pd_{50}	47.46	3.20	0.97 ± 0.04
TOH-Au@Pd_{60}	47.89	4.33	1.13 ± 0.05
TOH-Au@Pd_{80}	48.15	4.30	1.20 ± 0.05
TOH-Au@Pd_{120}	48.27	3.38	1.39 ± 0.05

lighter-contrast shell. The boundary between the core and shell is well-defined, exhibiting sharp contrast. Notably, faint step features characteristic of the Au {331} facets can be observed at the interface, as indicated by the red lines in the image. Further analysis of the lattice fringes reveals that the shell region displays a lattice spacing of approximately 0.225 nm, which is in good agreement with the (111) plane of face-centered cubic (fcc) Pd. In the core region, lattice spacings of approximately 0.236 and 0.144 nm are measured, corresponding to the (111) and (110) planes of fcc Au, respectively. This finding aligns with the description of the {331} facet as being composed of (111) and (110) components [32,33].

To accurately determine the shell thickness, statistical analysis was conducted on ten individual nanoparticles. For each particle, measurements were taken at three different locations, including vertices and edges, and the average value was calculated as the final shell thickness. The results indicate that at a Na_2PdCl_4 amount of 15 μL, the shell thickness is 0.54 nm, with some regions exhibiting incomplete Pd coverage (indicated by yellow circles in Fig. 1(b)). When the amount is increased to 30 μL, the shell thickness reaches 0.68 nm, with no obvious discontinuities observed (Fig. 1(d)). At an amount of 40 μL, a uniform and stable Pd shell is formed, with a thickness of 0.84 nm (Fig. 1(f)). As the Na_2PdCl_4 amount is further increased to 50, 60, 80, and 120 μL, continuous Pd shells are consistently formed, with the shell thickness progressively increasing to 0.97, 1.13, 1.20, and 1.39 nm, respectively (Table 1).

For clarity, the resulting nanoparticles are denoted as TOH-Au@Pd_x, where the subscript *x* represents the volume (in μL) of Na_2PdCl_4 solution used in the synthesis.

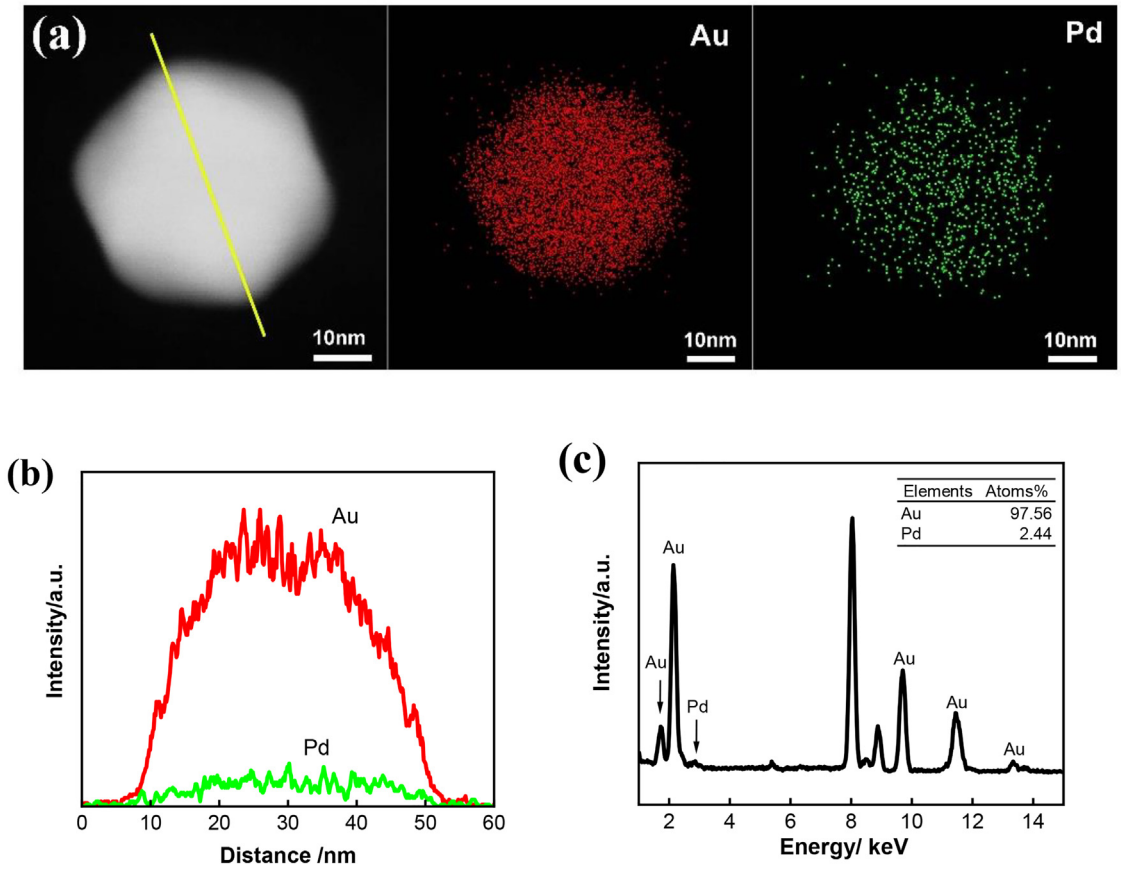

Fig. 2. HAADF-STEM-EDS mapping images (a), cross-sectional compositional line profile (b) and EDS spectrum (c) of a single TOH-Au@Pd_{40} NP. Red and green colors in image (a) and (b) represent the element Au and Pd, respectively.

High-angle annular dark-field scanning transmission electron microscopy coupled with energy-dispersive X-ray spectroscopy (HAADF-STEM-EDS) was employed to systematically characterize the elemental composition and distribution of individual TOH-Au@Pd_x nanoparticles, as shown in Figs. 2 and S2–S7. Elemental mapping (Fig. 2(a)) clearly shows that the nanoparticles are composed of Au and Pd. The Au signal (red) is predominantly localized in the nanoparticle interior, while the Pd signal (green) forms a continuous and uniform shell encapsulating the Au core. This distinct spatial distribution directly confirms the successful formation of the core-shell TOH-Au@Pd_x structure.

To further verify the core-shell structure, line-scan analysis was performed along the yellow line indicated in Fig. 2(a). The resulting line-scan profile (Fig. 2(b)) again confirms the coexistence of Au and Pd within the nanoparticle. It should be noted that the signal intensity of Pd is significantly lower than that of Au, which is consistent with the relatively small amount of Na_2PdCl_4 precursor used compared to the Au seeds, as expected.

In addition, quantitative elemental analysis was carried out using the corresponding EDS spectra (Fig. 2(c)). The results, summarized in Table 2, indicate that as the Na_2PdCl_4 addition was raised stepwise from 15 to 30, 40, 50, 60, 80, and 120 μL, the relative Pd content in the nanoparticles increased progressively from 1.17% to 2.04%, 2.44%, 2.70%, 4.71%, 4.94%, and 7.27%, respectively. This consistent progression confirms that a higher Na_2PdCl_4 supply effectively enhances the reduction and deposition of Pd^{2+} species on the TOH-Au surface, allowing fine-tuning of the Pd shell thickness in the resulting core-shell architecture.

The crystal structure and phase composition of TOH-Au@Pd_{40} and TOH-Au were examined by X-ray diffraction (XRD). As shown in Fig. 3, the XRD pattern of TOH-Au agrees well with the standard pattern for face-centered cubic (fcc) Au (JCPDS No. 04-0784). Distinct diffraction peaks corresponding to the (111), (200), (220), (311), and (222) planes are observed, confirming the well-defined crystalline nature of the synthesized TOH-Au sample.

Table 2
Atomic percentage of each element in the EDS spectrum.

Sample	Pd (%)	Au (%)
Au@Pd_{15}	1.17	98.83
Au@Pd_{30}	2.04	97.96
Au@Pd_{40}	2.44	97.56
Au@Pd_{50}	2.70	97.30
Au@Pd_{60}	4.71	95.29
Au@Pd_{80}	4.94	95.06
Au@Pd_{120}	7.27	92.73

Compared to TOH-Au, the XRD pattern of TOH-Au@Pd_{40} maintains a similar profile and peak distribution, while displaying a slight but consistent positive shift of all characteristic diffraction peaks toward higher angles. Since Au constitutes the major phase in TOH-Au@Pd_{40} with only a minor Pd content, this systematic peak shift can be explained by the partial substitution of Au atoms with smaller Pd atoms during shell formation, leading to a reduced lattice parameter [34,35]. According to Bragg's law, the consequent lattice contraction results in an increase in diffraction angle [36]. These results confirm that Pd is not only coated on the Au core surface to form a shell layer, but also partially incorporated into the Au lattice, resulting in atomic-scale alloying [37,38].

To probe the surface electronic structure and chemical states of the TOH-Au@Pd_x nanoparticles, X-ray photoelectron spectroscopy (XPS) measurements were conducted on TOH-Au@Pd_{15}, TOH-Au@Pd_{40},

Table 3
XPS shift of Pd 3d signals obtained from Pd NPs, TOH-Au@Pd_{15} NPs, TOH-Au@Pd_{40} NPs, and TOH-Au@Pd_{120} NPs.

Sample	Pd $3d_{5/2}$ peak (eV)	Pd $3d_{3/2}$ peak (eV)	ΔPd $3d_{5/2}$ peak (eV)	ΔPd $3d_{3/2}$ peak (eV)
Pd NPs	335.35	340.60	0	0
TOH-Au@Pd_{15} NPs	335.76	341.12	0.41	0.52
TOH-Au@Pd_{40} NPs	335.44	340.70	0.09	0.1
TOH-Au@Pd_{120} NPs	335.36	340.65	0.01	0.05

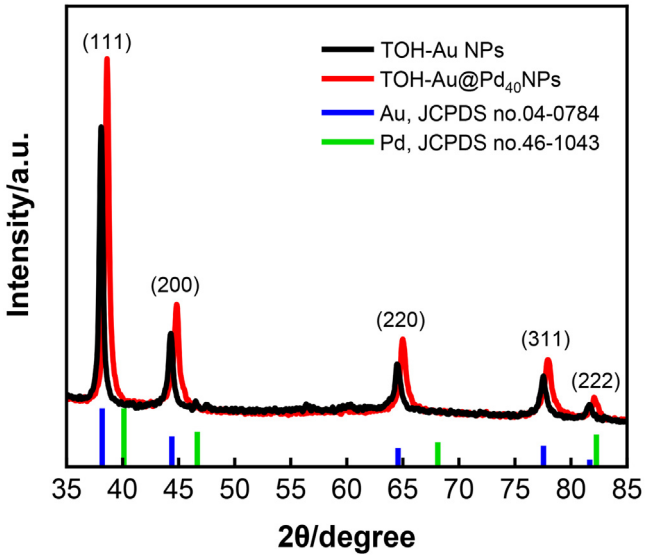

Fig. 3. XRD patterns of TOH-Au (black line) and TOH-Au@Pd_{40} NPs (red line).

TOH-Au@Pd_{120}, TOH-Au NPs, and pure Pd NPs for comparative analysis.

For TOH-Au NPs, the binding energies of the Au $4f_{7/2}$ and Au $4f_{5/2}$ core levels are located at 84.11 and 87.78 eV, respectively (Fig. S8 and Table S1). Upon the formation of TOH-Au@Pd_{15} NPs, both core levels shift negatively to 83.73 and 87.41 eV, corresponding to shifts of −0.38 and −0.37 eV, respectively. For TOH-Au@Pd_{40} NPs, the Au $4f_{7/2}$ and Au $4f_{5/2}$ binding energies are observed at 84.06 and 87.73 eV, with a negative shift of −0.05 eV. For TOH-Au@Pd_{120} NPs, the Au $4f_{7/2}$ and Au $4f_{5/2}$ binding energies are found at 84.1 and 87.77 eV, corresponding to a minimal negative shift of −0.01 eV.

In contrast, for pure Pd NPs, the Pd $3d_{5/2}$ and Pd $3d_{3/2}$ core levels are located at 335.35 and 340.60 eV, respectively (Fig. 4 and Table 3). Upon the formation of TOH-Au@Pd_{15} NPs, both core levels shift positively to 335.76 and 341.12 eV, with shifts of +0.41 and +0.52 eV, respectively. For TOH-Au@Pd_{40} NPs, the Pd $3d_{5/2}$ and Pd $3d_{3/2}$ binding energies are measured to be 335.44 and 340.70 eV, corresponding to positive shifts of +0.09 and +0.10 eV, respectively. For TOH-Au@Pd_{120} NPs, the binding energies of these two core levels are 335.36 and 340.65 eV, with shifts of +0.01 and +0.05 eV, respectively.

XPS analysis shows that after Pd shell coating, the Au 4f peaks shift to lower binding energy (negative shift), while the Pd 3d peaks shift to higher binding energy (positive shift). The shift values decrease as the shell thickness increases, as shown in Fig. 4(b). This indicates that thinner Pd shells induce a stronger interfacial electronic effect. As the shell thickens, this effect weakens, and the XPS signals gradually approach those of pure Pd.

This electronic effect is attributed to two factors: work function difference and ligand effect. Au has a higher work function than Pd. When they form a core-shell heterojunction, electrons transfer from Pd (lower work function) to Au (higher work function) to align the Fermi levels [39]. This electron transfer reduces the electron density on Pd (causing Pd 3d positive shifts) and increases it on Au (causing Au 4f negative shifts) [12]. Additionally, orbital hybridization between Pd and Au atoms at the interface (ligand effect) further modifies the Pd electronic structure. This short-range interaction is especially significant for ultrathin shells [39].

Extensive density functional theory (DFT) calculations have demonstrated that in core-shell structures, the d-band center of the shell metal is significantly modulated by the core metal [40–43]. DFT studies reveal that this modulation is primarily governed by two mechanisms: (1) Ligand effect: orbital hybridization between the core and shell metals directly modifies the electronic density of states of the shell metal, leading to a shift in the d-band center [39]; (2) Strain effect: lattice mismatch between the core and shell generates strain that also influences the d-band center position [39,44]. For the Au@Pd system, DFT calculations reveal that when the Pd shell is thin, the combined effects of the ligand effect and tensile strain induced by lattice mismatch cause a significant upshift of the Pd d-band center toward the Fermi level [43]. As the shell thickness increases, these interfacial effects are progressively screened, and the d-band center gradually returns to a position close to that of bulk Pd [43].

Based on the aforementioned DFT consensus and our XPS experimental data, a correlation can be established between the binding energy shifts and the D-band center variation. XPS binding energy shifts reflect changes in the local electron density around the atoms, and such changes are intrinsically linked to shifts in the d-band center [45]. In our system, the positive shift of the Pd 3d core level indicates electron depletion and a decrease in the local electron density of Pd. According to the d-band center model, a decrease in electron density leads to a narrowing and upshift of the d-band, bringing the d-band center closer to the Fermi level. It is important to note that while core-level shifts probe the binding energy of inner-shell electrons, the d-band center describes the average energy of valence d-electrons; these two are related but not equivalent. For the Au@Pd core-shell system, previous studies combining XPS valence band spectroscopy and DFT calculations have demonstrated a good correlation between the trend of the Pd d-band center and the core-level shifts [46].

Based on the above analysis, the evolution of the d-band center with increasing shell thickness can be summarized as follows.

When the Pd shell is extremely thin, nearly all Pd atoms are in direct contact with the Au substrate and experience strong interfacial electronic perturbations. The combined effects of work-function-difference-driven charge transfer and the ligand effect result in a significant upshift of the Pd d-band center toward the Fermi level, accompanied by the largest observed XPS binding energy shifts. As the shell thickness increases, the interfacial electronic effect gradually weakens, and the d-band center progressively shifts back, with a corresponding decrease in the binding energy shifts. When the shell becomes sufficiently thick, most Pd atoms are far from the interface, and their electronic structure increasingly resembles that of bulk Pd. The d-band center returns to its intrinsic position, and the binding energy shifts become minimal, approaching the values characteristic of pure Pd.

Additionally, peak-area analysis of the Pd 3d region in TOH-Au@Pd_{40} yields a Pd $3d_{5/2}$-to-Pd $3d_{3/2}$ ratio of approximately 3.7:1, which markedly exceeds the theoretical ratio of 3:2. This deviation can be explained by the overlap of the Au $4d_{5/2}$ peak located near 335 eV, which contributes to the integrated intensity of the Pd $3d_{5/2}$ signal [35].

The electronic interaction arising from the core-shell structure is regarded as a crucial factor for the enhanced electrocatalytic performance [47,48]. Indeed, subsequent ethanol electrooxidation tests show that

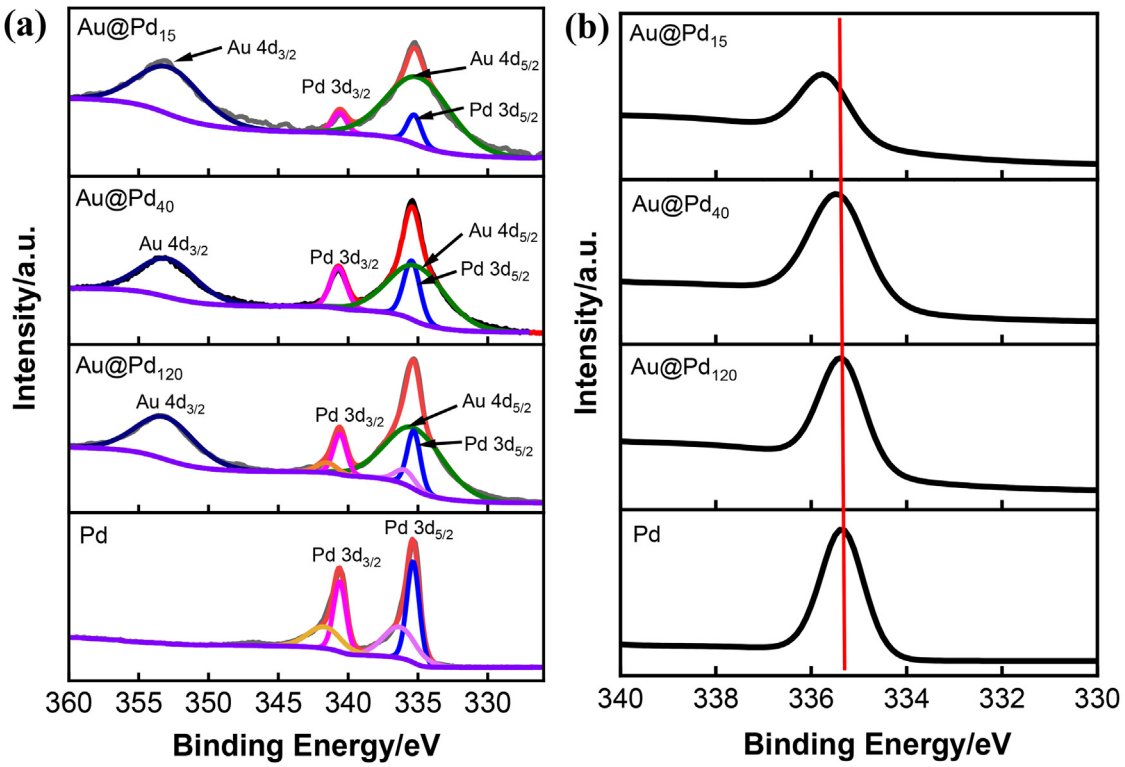

Fig. 4. (a) XPS spectra of Pd 3d signals obtained from Pd NPs, TOH-Au@Pd_{15} NPs, TOH-Au@Pd_{40} NPs, and TOH-Au@Pd_{120} NPs. (b) Corresponding enlarged view of the Pd $3d_{5/2}$ peaks.

TOH-Au@Pd_{40} delivers substantially higher activity than both TOH-Au NPs and commercial Pd/C, confirming that the modulation of the electronic structure effectively promotes the catalytic behavior.

3.2. Electrocatalytic performance of TOH-Au@Pd_x NPs in ethanol oxidation

To systematically investigate the influence of Pd shell content on electrocatalytic performance, the ethanol electro-oxidation performance of a series of TOH-Au@Pd_x nanoparticles with different Pd loadings and commercial Pd/C catalyst was comprehensively evaluated and compared in alkaline media.

Fig. 5(a) displays the cyclic voltammetry (CV) curves of the samples recorded in 0.5 mol/L KOH solution. The reduction peak observed around −0.2 V is assigned to the reduction of Pd species, while the peak near 0.1 V corresponds to the reduction of surface Au oxide (Fig. S9) [49]. To better compare the reduction features near 0.1 V, an enlarged view of this region is provided in Fig. 5(b).

The enlarged CV view (Fig. 5(b)) shows that with 15 μL of Na_2PdCl_4, a distinct Au reduction peak is observed, indicating incomplete Pd-shell coverage and significant exposure of Au sites to the electrolyte. Increasing the Na_2PdCl_4 amount to 30 μL substantially weakens the Au peak, leaving only a broad, low-intensity feature, which suggests that the Au surface is largely covered by Pd and the number of accessible Au sites is greatly reduced. At 40 μL of Na_2PdCl_4, the Au reduction peak disappears completely, and the CV curve becomes smooth in this potential range, confirming full encapsulation of the Au core by the Pd shell and the absence of exposed Au sites. This progressive attenuation of the Au reduction signal clearly illustrates that higher Na_2PdCl_4 amounts lead to increased Pd coverage on the TOH-Au surface, culminating in a well-defined core-shell structure.

The electrochemical active surface area (ECSA) of the catalyst series was determined from double-layer capacitance measurements, employing an adsorption charge density of 4.3 C/m^2 associated with Pd-oxide reduction [49,50]. The obtained ECSA values are listed in Table 4. With increasing Na_2PdCl_4 amount, the ECSA first rises and then falls, showing a distinct volcano-shaped dependence. A maximum ECSA of 128.8 m^2/g is achieved at a Na_2PdCl_4 amount of 40 μL, suggesting that the Pd shell formed under this condition achieves an optimal balance between atomic dispersion and the accessibility of active sites.

The ethanol electro-oxidation reaction of the synthesized TOH-Au@Pd_x NPs was further examined in alkaline electrolyte. An oxidation peak near 0.2 V is visible in Fig. 5(c), attributable to ethanol oxidation on exposed Au surfaces (the catalytic curve of pure TOH-Au NPs is provided in Fig. S9). Significantly, when 40 μL of Na_2PdCl_4 is used, this Au-associated oxidation peak disappears completely, providing further strong support for the complete coverage of the Au core by the Pd shell.

As summarized in Table 4, the mass activity for ethanol oxidation also displays a characteristic volcano-shaped dependence on the Na_2PdCl_4 amount, reaching a maximum of 13.6 A/mg at 40 μL. The specific activity, calculated from the corresponding ECSA values, follows a similar trend.

According to the d-band center model proposed by Hammer and Nørskov, the adsorption energy of reaction intermediates on metal surfaces is closely correlated with the position of the d-band center relative to the Fermi level [51]. In the Au@Pd core-shell structure, lattice mismatch and the ligand effect between the Au core and Pd shell induce a shift in the d-band center of the Pd shell, thereby modulating its intrinsic catalytic activity [39]. Based on the Sabatier principle, optimal catalytic activity requires that the adsorption of reaction intermediates is neither too strong (which would hinder product desorption) nor too weak (which would make reactant activation difficult) [52]. In other words, the d-band center must be positioned at an “optimal” energy.

Based on this theoretical framework, a mechanistic interpretation for the volcano-shaped trend of catalytic activity with increasing Pd shell thickness is proposed as follows.

When the Pd shell is extremely thin, the interfacial electronic effect is most pronounced, causing a significant upshift of the Pd d-band cen-

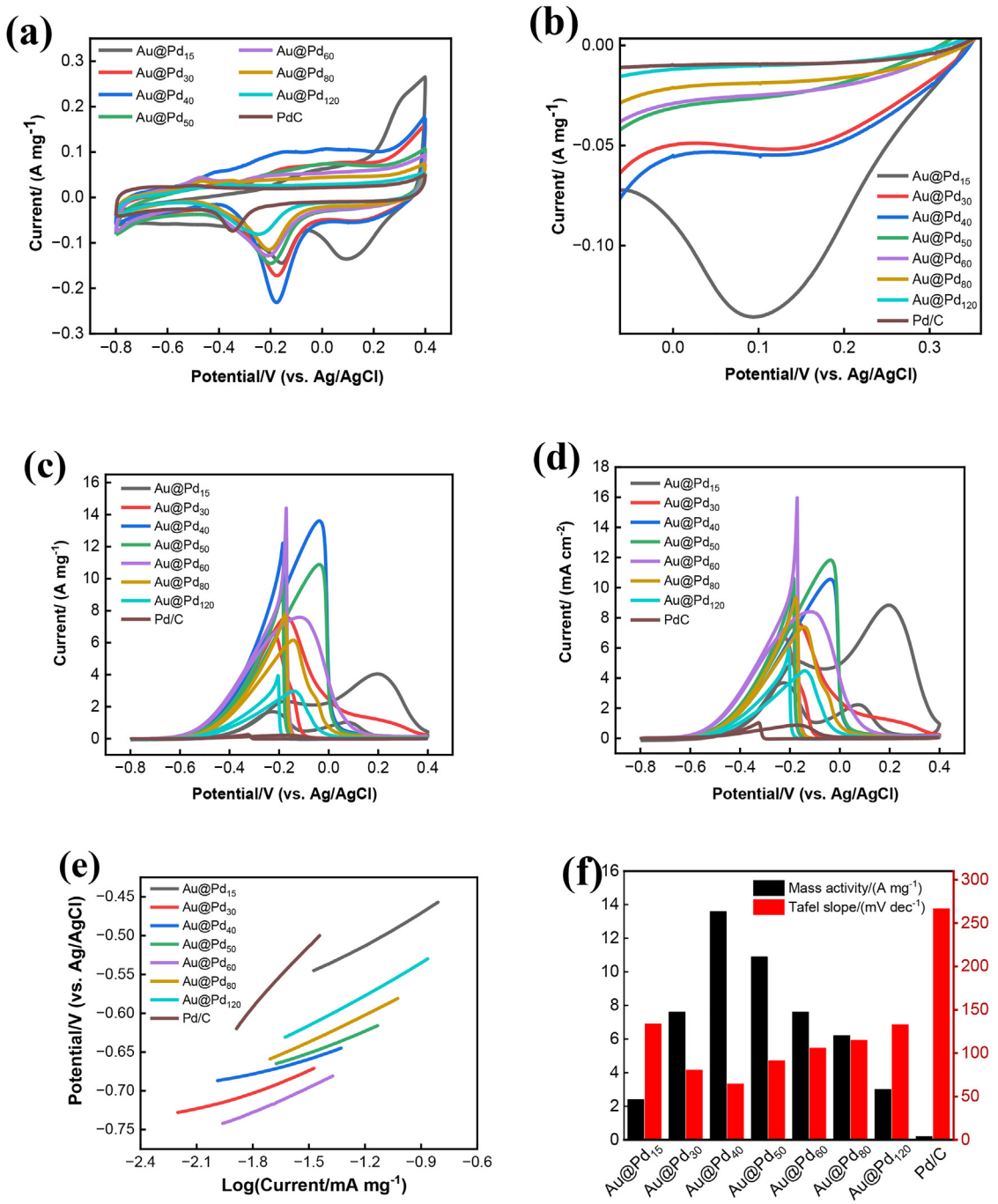

Fig. 5. CVs of TOH-Au@Pd$_x$ NPs measured in 0.5 mol/L KOH. (a) Without ethanol; (b) Magnified view of the redox features in (a). (c) With 0.5 mol/L ethanol; (d) CVs in (c) normalized by ECSA. Currents in (a)–(c) are normalized by Pd mass loading on the glassy carbon electrode (GCE). Scan rates: 50 mV/s for (a)(b) and 20 mV/s for (c)(d). (e) Tafel plots of TOH-Au@Pd$_x$ NPs measured in 0.5 mol/L KOH containing 0.5 mol/L ethanol. (f) Histograms comparing the mass activity and Tafel slope of TOH-Au@Pd$_x$ catalysts and commercial Pd/C.

Table 4
Summary of ethanol oxidation performance for TOH-Au@Pd$_x$ NPs.

Sample	Mass activity/ (A mg^{-1})	ECSA/(m^2 g^{-1})	Specific activity/(mA cm^{-2})	Tafel slope (mV dec^{-1})
Au@Pd$_{15}$	2.4	45.9	5.2	133.6
Au@Pd$_{30}$	7.6	98.8	7.7	80.4
Au@Pd$_{40}$	13.6	128.8	10.6	64.5
Au@Pd$_{50}$	10.9	92.0	11.8	91.2
Au@Pd$_{60}$	7.6	90.3	8.4	105.7
Au@Pd$_{80}$	6.2	83.3	7.4	114.8
Au@Pd$_{120}$	3.0	66.5	4.5	132.8
Pd/C	0.2	25.7	0.8	266.4

ter toward the Fermi level. According to the d-band center model, an upshift of the d-band center enhances the bonding strength between adsorbates and the metal surface. While this facilitates reactant activation, it also leads to excessively strong binding of reaction intermediates and poisonous species such as CO_{ads} [53]. Such overly strong adsorption hinders product desorption and leads to persistent occupation of active sites. Consequently, despite the strong electronic effect, the intrinsic activity is not optimal.

As the shell thickness increases to an optimal value, the interfacial electronic effect weakens to a moderate level, positioning the d-band center at an optimal energy. This moderate d-band position achieves an ideal balance between reactant activation and product desorption: it maintains sufficient binding affinity for reactants to ensure efficient activation while preventing excessive accumulation of intermediates. As a result, the intrinsic activity reaches its maximum, precisely located at the "volcano apex" predicted by d-band center theory.

When the shell thickness further increases, the interfacial electronic effect continues to diminish, and the d-band center gradually shifts back toward its intrinsic position in bulk Pd. This downshift of the d-band center weakens the adsorption energy of reaction intermediates, leading to reduced reactant activation capability and slower reaction kinetics [54]. Consequently, the catalytic activity progressively declines.

Therefore, the Pd shell thickness continuously modulates the d-band center position by regulating the strength of the interfacial electronic effect, thereby governing the adsorption strength of reaction intermediates. As the shell thickness increases, the d-band center undergoes a continuous evolution from "excessively high-optimal-reverting to the intrinsic value". Correspondingly, the catalytic activity exhibits a volcano-shaped trend of first increasing and then decreasing, which is in excellent agreement with the theoretical predictions of the d-band center model.

A systematic performance comparison was carried out between the TOH-Au@Pd_x series and commercial Pd/C to fully assess the advantages of the synthesized catalysts. All TOH-Au@Pd_x catalysts show substantially higher electrochemical active surface area (ECSA), mass activity, and specific activity than commercial Pd/C. The optimal sample, TOH-Au@Pd_{40}, delivers an ECSA of 128.8 m^2/g, a mass activity of 13.6 A/mg, and a specific activity of 10.6 mA/cm^2, which represent improvements by factors of 5.0, 68.0, and 13.3, respectively, relative to commercial Pd/C. Furthermore, the mass activity of TOH-Au@Pd_{40} is 272 times higher than that of pure TOH-Au NPs (0.05 A/mg, Fig. S9), underscoring the essential contribution of the Au-Pd core-shell architecture to the enhanced catalytic performance.

To further demonstrate the advancement of this work, a direct comparison was made with several representative Au@Pd catalysts reported in the literature. The mass activity of TOH-Au@Pd_{40} reaches 1.5 times that of cubic Au@Pd_{1L} (9.0 A/mg) [35], 2.0 times that of Au@Pd nanorods (6.82 A/mg) [55], and 3.3 times that of spherical Au@$Pd_{0.55}$ nanoparticles (4.14 A/mg) [19], highlighting its superior activity. The outstanding electrocatalytic performance can be primarily attributed to the unique trisoctahedral architecture enclosed by high-index {331} facets. This structure exposes a high density of catalytically active sites, including steps, edges, and kinks, which substantially enhance reactant adsorption and facilitate efficient activation [31,56]. Concurrently, the electronic synergy between the TOH-Au core and the Pd shell further optimizes the electronic structure of the surface Pd atoms, collectively promoting the ethanol electro-oxidation reaction.

To evaluate the reaction kinetics of the as-prepared catalysts, the corresponding Tafel slopes were calculated and are presented in Figs. 5(e)(f) and Table 4. The results show that all TOH-Au@Pd_x catalysts exhibit substantially lower Tafel slopes than that of Pd/C. As the Pd shell thickness increases, the Tafel slope first decreases and then increases, with TOH-Au@Pd_{40} NPs displaying the smallest value (64.5 mV/dec). This indicates that an optimal Pd shell thickness is most favorable for enhancing the reaction kinetics.

To further investigate the interfacial charge transfer kinetics, electrochemical impedance spectroscopy (EIS) measurements were performed on the as-prepared catalysts, with the results shown in Fig. S11. In Nyquist plots, the diameter of the semicircle is closely related to the charge transfer resistance: a smaller semicircle diameter corresponds to lower charge transfer resistance and faster reaction kinetics. It can be clearly observed that all TOH-Au@Pd_x catalysts exhibit significantly smaller semicircle diameters than commercial Pd/C. Notably, TOH-Au@Pd_{40} displays the smallest semicircle diameter among all samples, indicating the lowest charge transfer resistance and thus the most favorable interfacial charge transfer kinetics. Consistent with this, TOH-Au@Pd_{40} also exhibits the smallest Tafel slope and the smallest charge transfer resistance, further confirming its optimal reaction kinetics and interfacial charge transfer capability, which aligns well with its highest catalytic activity.

To comprehensively evaluate the electrochemical stability of the catalysts, two distinct durability tests were conducted: accelerated durability testing via cyclic voltammetry and long-term durability testing via chronoamperometry.

First, the TOH-Au@Pd_{40} catalyst, which exhibited optimal catalytic activity, was subjected to accelerated durability testing through 500 consecutive cyclic voltammetry scans. As shown in Fig. 6(a), the catalyst retained 80.3% of its initial activity after 500 cycles. Post-cycling HRTEM characterization (Fig. S12) revealed noticeable nanoparticle adhesion and aggregation. High-resolution images confirmed that the core-shell structure was preserved, with distinct lattice fringes corresponding to Pd and Au clearly observable, indicating that the phase composition of the sample remained unchanged. However, the Pd shell thickness decreased from an initial average of 0.84 to 0.63 nm. Therefore, the observed nanoparticle adhesion and shell thinning are likely the primary factors contributing to the activity decay.

Subsequently, chronoamperometric (*I-t*) measurements were performed at a fixed potential for 7200 s to assess the long-term durability of three representative catalysts: the optimally active TOH-Au@Pd_{40}, the thinnest-shelled TOH-Au@Pd_{15}, and the thickest-shelled TOH-Au@Pd_{120}. The results are presented in Fig. 6(b). All TOH Au@Pd_x catalysts demonstrated significantly superior stability compared to PdC, which retained only 1.4% of its initial activity. Among them, TOH-Au@Pd_{40} NPs exhibited the highest activity retention (27.5%), while TOH-Au@Pd_{15} NPs (10.2%) and TOH-Au@Pd_{120} NPs (11.9%) showed more pronounced degradation.

This difference in stability can be attributed to the synergistic regulation of structural integrity and anti-poisoning capability by the shell thickness:

For TOH-Au@Pd_{15}, the incomplete shell (indicated by yellow circles in Fig. 1(b)) introduces structural defects that serve as initiation sites for Pd dissolution or Ostwald ripening during prolonged electrolysis [57]. Moreover, the incomplete shell fails to effectively protect the Au core, leading to interfacial reconstruction and accelerated activity decay.

For TOH-Au@Pd_{40}, the continuous and uniform shell provides an effective structural barrier that suppresses Pd dissolution and migration [58]. Simultaneously, the moderate interfacial electronic effect optimizes the electronic structure of Pd, reducing the accumulation tendency of poisonous species (e.g. CO_{ads}) on active sites [59]. The synergy between these two factors endows TOH-Au@Pd_{40} with optimal stability.

For TOH-Au@Pd_{120}, despite its structural integrity, the interfacial electronic effect is substantially weakened, rendering the Pd electronic structure similar to that of bulk Pd. This results in insufficient promotion of poisonous species desorption, leading to their accumulation and persistent occupation of active sites [60]. Additionally, internal stress within the thick shell may induce lattice defects or shell detachment during electrolysis, further accelerating deactivation [61].

The superior stability of all core-shell catalysts compared to commercial Pd/C can be attributed to the electronic synergy between the Au core and Pd shell, as well as the structural robustness provided by the core-shell architecture. This effectively mitigates the dissolution, ag-

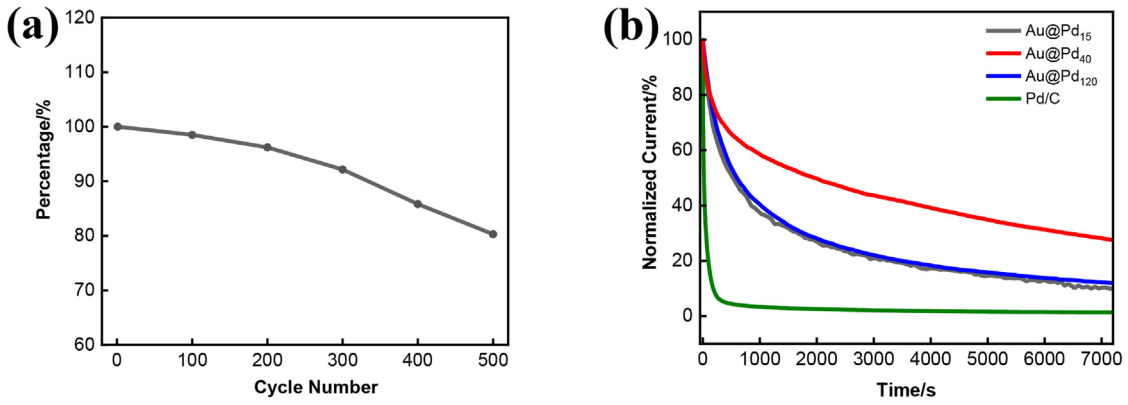

Fig. 6. (a) Normalized anodic peak current retention of TOH-Au@Pd_{40} NPs during cyclic voltammetry cycling in 0.5 mol/L KOH containing 0.5 mol/L ethanol. (b) Chronoamperometric (*I-t*) curves of TOH-Au@Pd_{15}, TOH-Au@Pd_{40}, TOH-Au@Pd_{120}, and commercial Pd/C recorded at −0.3 V in 0.5 mol/L KOH and 0.5 mol/L ethanol for 7200 s.

gregation, and poisoning mechanisms commonly observed in conventional Pd catalysts. Therefore, the optimal shell thickness achieves the best balance between structural integrity and electronic effect, thereby exhibiting the highest activity retention during long-term operation.

Moreover, literature values for Au@Pd nanorods and Au@$Pd_{0.1}$/C show retained currents of 3.3% (after 3600 s) [55] and 8% (after 1800 s) [6], respectively. These comparisons clearly indicate that TOH-Au@Pd_{40} possesses superior poisoning resistance and durability, outperforming both commercial Pd/C and other reported Au@Pd catalysts.

4. Conclusions

In this study, a series of TOH-Au@Pd_x core-shell nanoparticles with precisely controlled Pd shell thicknesses were successfully constructed using TOH-Au with a diameter of approximately 45 nm as seeds, by carefully adjusting the amount of Na_2PdCl_4 precursor. Structural characterization confirmed that the as-prepared nanoparticles exhibit well-defined morphology and excellent monodispersity, with average particle sizes distributed in the range of 46.5–48.5 nm. As the Na_2PdCl_4 volume increased from 15 to 120 μL, the Pd shell thickness progressively increased from 0.54 to 1.39 nm. At a volume of 40 μL, the Pd shell completely enveloped the Au core, forming an ideal core-shell structure. XPS analysis reveals that the Au 4f peaks shift to lower binding energies, while the Pd 3d peaks shift to higher binding energies. The magnitude of these shifts progressively decreases with increasing Pd shell thickness. This phenomenon confirms electron transfer from the Pd shell to the Au core, demonstrating significant electronic interaction between the two metals that weakens as the shell thickens. Such optimal electronic synergy effectively modulates the adsorption behavior of reaction intermediates, thereby enhancing the electrocatalytic performance of the catalysts. Electrochemical evaluation demonstrated that all TOH-Au@Pd_x catalysts exhibited superior catalytic performance for the alkaline ethanol oxidation reaction compared to commercial Pd/C. Among them, TOH-Au@Pd_{40} displayed the most exceptional performance, with an electrochemical surface area of 128.8 m^2/g, a mass activity of 13.6 A/mg, and a specific activity of 10.6 mA/cm^2, which are 5.0, 68.0, and 13.3 times higher than those of commercial Pd/C, respectively. TOH-Au@Pd_{40} also exhibited the smallest Tafel slope and charge transfer resistance, indicating its most favorable reaction kinetics. Stability tests revealed that TOH-Au@Pd_{40} retained 27.5% of its initial activity after 7200 s of continuous operation, significantly outperforming commercial Pd/C (1.4%), demonstrating substantially enhanced anti-poisoning capability and durability. The excellent electrocatalytic performance can be attributed to the high-index facets (containing highly active sites such as steps, edges, and kinks) provided by the trisoctahedral Au core, in synergy with the optimal electronic interaction between the Au core and Pd shell. This study provides an effective strategy for the controlled synthesis of highly active core-shell catalysts and systematically reveals how shell thickness regulates electronic structure, catalytic activity, and stability. These insights offer a theoretical basis for understanding the structure-activity relationship and catalytic enhancement mechanism of core-shell catalysts.

Declaration of Competing Interest

The authors declare that they have no known competing financial interests or personal relationships that could have appeared to influence the work reported in this paper.

CRediT authorship contribution statement

Li Kong: Writing – review & editing, Writing – original draft, Supervision, Funding acquisition, Data curation.

Acknowledgements

This work was financially supported by the Instrument Improvement Funds of Shandong University (No. ts20250301) and the Laboratory Construction and Management Research Project of Shandong University (No. sy20213206).

Supplementary materials

Supplementary material associated with this article can be found, in the online version, at doi:10.1016/j.chphma.2026.04.002.

References

[1] D. Saritha, N.M. Reddy, G.V. Ramesh, Pt- and Pd- based intermetallic anode catalysts for direct ethanol fuel cell (DEFC): An overview, Mater. Today: Proc. 64 (2022) 357–362, doi:10.1016/j.matpr.2022.04.705.
[2] A.L. De Bortoli, A two-phase stable model for non-isothermal direct ethanol proton exchange membrane fuel cells, J. Power Sources 659 (2025) 238394–238401, doi:10.1016/j.jpowsour.2025.238394.
[3] M. Roschger, S. Wolf, A. Billiani, S. Gorgieva, B. Genorio, V. Hacker, Electrode configurations study for alkaline direct ethanol fuel cells, J. Electrochem. Sci. Eng. 13 (2023) 783–793, doi:10.5599/jese.1623.
[4] J. Kaur, R.K. Gupta, A. Kumar, Electrocatalytic ethanol oxidation reaction: Recent progress, challenges, and future prospects, Discover Nano 19 (2024) 137–155, doi:10.1186/s11671-024-04067-9.
[5] S.G.M. Carvalho, F.N. Tabuti, E.I. Santiago, R. Abe, R.M. Guimaraes, Y. Miura, Y. Fukuyama, F.C. Fonseca, Advancing direct ethanol metal supported fuel cells with catalytic layer, Mater. Sci. Eng. B 318 (2025) 118259–118302, doi:10.1016/j.mseb.2025.118259.
[6] J.G. Ruiz-Montoya, L.M.S. Nunes, A.M. Baena-Moncada, G. Tremiliosi-Filho, J.C. Morales-Gomero, Effect of palladium on gold in core-shell catalyst for electrooxidation of ethanol in alkaline medium, Int. J. Hydrogen Energy 46 (2021) 23670–23681, doi:10.1016/j.ijhydene.2021.04.159.

[7] Z.F. Wu, R.B. Duan, J.L. Cui, C.P. Ye, S.C. Zhang, S.H. Yan, An overview of the Pd based electrocatalysts utilized in direct alcohol fuel cells, Electrocatalysis 16 (2025) 197–223, doi:10.1007/s12678-024-00920-8.
[8] Y. Zheng, X.J. Wan, X. Cheng, K. Cheng, Z.F. Dai, Z.H. Liu, Advanced catalytic materials for ethanol oxidation in direct ethanol fuel cells, Catalysts 10 (2020) 166–188, doi:10.3390/catal10020166.
[9] H. Wu, Z.C. Mao, B.Q. Liu, D.Y. Chen, M.Q. Shi, B.S. Lv, Y.H. Xu, L.B. Wang, Ultra-low-loading Pd nanocrystals modified Ni foam electrode for efficient electrochemical hydrodechlorination, Appl. Catal. B 337 (2023) 122978–122988, doi:10.1016/j.apcatb.2023.122978.
[10] R.M. Zhu, Y.X. Jiang, Y.Z. Song, L.M. Liu, Y.H. Xu, H. Pang, Recent progress in core-shell structural materials towards high performance batteries, Chem. Eng. J. 490 (2024) 151681–151717, doi:10.1016/j.cej.2024.151681.
[11] W.J. Lu, X.T. Guo, Y.Q. Luo, Q. Li, R.M. Zhu, H. Pang, Core-shell materials for advanced batteries, Chem. Eng. J. 355 (2019) 208–237, doi:10.1016/j.cej.2018.08.132.
[12] D.P. Chen, Z.Y. Shao, L.R. Yang, Y. Chen, Y.H. Wei, Z.H. Hu, L.Y. Cai, Y.F. Zhang, X. He, A special carbon core@Au/Pd shell structure catalyst: Au-Pd layer on the mesoporous carbon microsphere for enhanced activity of ethanol electro-oxidation, Int. J. Hydrogen Energy 87 (2024) 107–116, doi:10.1016/j.ijhydene.2024.08.495.
[13] Y.Y. Liang, Q. Wu, F. Liang, Analysis of catalytic activity of Au@Pd core-shell nanodendrites for highly efficient ethanol electrooxidation, Chin. J. Anal. Chem. 49 (2021) E21087–E21095, doi:10.1016/s1872-2040(21)60103-2.
[14] T.L. Guo, S.T. Bao, J. Guo, W. Chen, L.L. Wen, Bimetallic Au-Pd NPs embedded in MOF ultrathin nanosheets with tuned surface electronic properties for high-performance benzyl alcohol oxidation, Chem. Res. Chin. Univ. 38 (2022) 1344–1348, doi:10.1007/s40242-022-2210-y.
[15] G.G. Zhang, Y.Y. Ma, X.W. Fu, W.J. Zhao, F. Liu, M.C. Liu, Y.Q. Zheng, Enriching the branching of Au@PdAu core-shell nanocrystals using a syringe pump: Kinetics control meets lattice mismatch, CrystEngComm 23 (2021) 2582–2589, doi:10.1039/d1ce00107h.
[16] J.F. Hao, B. Liu, M. Takahashi, S. Maenosono, J.H. Yang, Large Au@Pd/PdO_x core-porous shell nanoparticles as efficient ethanol oxidation electrocatalysts, Catal. Sci. Technol. 13 (2023) 4141–4147, doi:10.1039/d3cy00637a.
[17] P. Gnanaprakasam, A. Gowrisankar, S. Senthilkumar, A. Murugadoss, T. Selvaraju, R.V. Mangalaraja, One pot in situ synthesis of nano Au-Pd core-shells embedded on reduced graphene oxide for the oxygen reduction reaction, Mater. Sci. Eng. B 264 (2021) 114924–114934, doi:10.1016/j.mseb.2020.114924.
[18] H. Liu, H. Wang, H.C. Ma, B. Liu, J.H. Yang, Au core-porous Pd shell loaded Au nanoparticles superstructures as efficient electrocatalysts for ethanol oxidation reaction, Mater. Res. Bull. 188 (2025) 113406–113413, doi:10.1016/j.materresbull.2025.113406.
[19] Y. Dai, Z. Xie, Y. Zhang, X. Du, Z. Li, J. Xie, Z. Sun, J. Zhou, Mapping surface and subsurface atomic structures of Au@Pd core-shell nanoparticles in three dimensions, ACS Nano 19 (2025) 9006–9016, doi:10.1021/acsnano.4c17462.
[20] H.F. Huang, A. Yamamoto, R. Sugiyama, A. Tanaka, H. Kominami, H. Yoshida, Core-shell Au@Pd cocatalyst for efficient and selective photocatalytic synthesis of deuterated alkanes from lauric acid and heavy water, Catal. Today 461 (2026) 115520–115528, doi:10.1016/j.cattod.2025.115520.
[21] K. Ramesh, G.B. Reddy, C. Raghavender, V. Gopi, M. Noorjahan, Biogenic synthesis of gold-palladium bimetallic nanoparticles using Passiflora edulis fruit peel extract for catalytic reduction of rhodamine B and methyl orange dyes, React. Kinet. Mech. Catal. 138 (2025) 4259–4272, doi:10.1007/s11144-025-02945-6.
[22] P. Singh, P.K.Gangadharan Sonika, Z. Khan, S. Kurungot, A. Jaiswal, Cubic palladium nanorattles with solid octahedron gold core for catalysis and alkaline membrane fuel cell applications, Chemcatchem 11 (2019) 4383–4392, doi:10.1002/cctc.201900741.
[23] C. Fernández-Navarro, S. Mejía-Rosales, Stability of Au-Pd core-shell nanoparticles, J. Phys. Chem. C 121 (2017) 21658–21664, doi:10.1021/acs.jpcc.7b04564.
[24] Z.H. Ye, B. Shen, D.H. Kang, J. Huang, Z. Wang, C.B. Wahl, D. Shin, L.L. Huang, J.H. Shen, C.M. Wolverton, C.A. Mirkin, Using surface composition and energy to control the formation of either tetrahexahedral or hexoctahedral high-index facet nanostructures, J. Am. Chem. Soc. 146 (2024) 13519–13526, doi:10.1021/jacs.4c03088.
[25] N. Goubet, J.H. Yang, P.A. Albouy, M.P. Pileni, Spontaneous formation of high-index planes in gold single domain nanocrystal superlattices, Nano Lett. 14 (2014) 6632–6638, doi:10.1021/nl503289a.
[26] B. Shen, L.L. Huang, J.H. Shen, K. He, C.Y. Zheng, V.P. Dravid, C. Wolverton, C.A. Mirkin, Crystal structure engineering in multimetallic high-index facet nanocatalysts, Proc. Natl. Acad. Sci. U.S.A. 118 (2021) e2105722118 e2105722124, doi:10.1073/pnas.2105722118.
[27] J. Carnis, L. Gao, S. Fernández, G. Chahine, T.U. Schulli, S. Labat, E.J.M. Hensen, O. Thomas, J.P. Hofmann, M.I. Richard, Facet-dependent strain determination in electrochemically synthetized platinum model catalytic nanoparticles, Small 17 (2021) 2007702–2007712, doi:10.1002/smll.202007702.
[28] K. Huang, R.M. Crooks, Enhanced electrocatalytic activity of Cu-modified, high-index single Pt NPs for formic acid oxidation, Chem. Sci. 13 (2022) 12479–12490, doi:10.1039/d2sc03433f.
[29] L. Kong, M. Hao, L. Li, Synthesis of small-sized trisoctahedral gold nanoparticles with high catalytic activity for methanol electrooxidation, Chem. Res. Chin. Univ. 41 (2025) 903–909, doi:10.1007/s40242-025-5003-2.
[30] Y. Song, M. Zhang, H. Fang, H. Xia, Shape transformation of gold nanoparticles in aqueous CTAB/CTAC solution to generate high-index facets for electrocatalysis and SERS activity, ChemPhysMater 2 (2023) 97–113, doi:10.1016/j.chphma.2022.04.006.
[31] Z.W. Quan, Y.X. Wang, J.Y. Fang, High-index faceted noble metal nanocrystals, Acc. Chem. Res. 46 (2013) 191–202, doi:10.1021/ar200293n.
[32] Y.H. Song, T.T. Miao, P.N. Zhang, C.X. Bi, H.B. Xia, D.Y. Wang, X.T. Tao, {331}-Faceted trisoctahedral gold nanocrystals: Synthesis, superior electrocatalytic performance and highly efficient SERS activity, Nanoscale 7 (2015) 8405–8415, doi:10.1039/c5nr01049g.
[33] F. Xue, X. Guo, B. Min, Y. Si, H. Huang, J. Shi, M. Liu, Unconventional high-index facet of iridium boosts oxygen evolution reaction: How the facet matters, ACS Catal. 11 (2021) 8239–8246, doi:10.1021/acscatal.1c01867.
[34] Z. Li, S.F. Ji, Y.W. Liu, X. Cao, S.B. Tian, Y.J. Chen, Z.G. Niu, Y.D. Li, Well-defined materials for heterogeneous catalysis: From nanoparticles to isolated single-atom sites, Chem. Rev. 120 (2020) 623–682, doi:10.1021/acs.chemrev.9b00311.
[35] Y.H. Song, C.S. Xiang, C.X. Bi, C.S. Wu, H.P. He, W. Du, L.H. Huang, H. Tian, H.B. Xia, PH-dependent growth of atomic Pd layers on trisoctahedral gold nanoparticles to realize enhanced performance in electrocatalysis and chemical catalysis, Nanoscale 10 (2018) 22302–22311, doi:10.1039/c8nr07224h.
[36] J.T.L. Gamler, A. Leonardi, X.H. Sang, K.M. Koczkur, R.R. Unocic, M. Engel, S.E. Skrabalak, Effect of lattice mismatch and shell thickness on strain in core@shell nanocrystals, Nanoscale Adv. 2 (2020) 1105–1114, doi:10.1039/d0na00061b.
[37] K.N. da Silva, S. Shetty, S. Sullivan-Allsop, R.S. Cai, S.Q. Wang, J. Quiroz, M. Chundak, H.L.S. dos Santos, I. Abdelsalam, F.E. Oropeza, V.A.D. O'Shea, N. Heikkinen, E. Sitta, T.V. Alves, M. Ritala, W.Y. Huo, T.J.A. Slater, S.J. Haigh, P.H.C. Camargo, Au@AuPd core-alloyed shell nanoparticles for enhanced electrocatalytic activity and selectivity under visible light excitation, ACS Nano 18 (2024) 24391–24403, doi:10.1021/acsnano.4c07076.
[38] S.D. Ji, Q. Wang, J.P. Huang, R.Y. Guo, Y.N. Li, Y.Z. Zheng, R. Li, Y.H. Zhao, C. Wu, M.S. Jin, Electrochemical CO_2 reduction via strain-engineered AuPd alloy catalysts, Chem. Eng. J. 520 (2025) 166114 16122, doi:10.1016/j.cej.2025.166114.
[39] S.T. Tanuja, T. Singha, B. Satpati, Tuning the d-band center via strain and ligand effects in core-shell pentatwinned Au@Pd nanoparticles for enhanced ethanol oxidation reaction, Adv. Funct. Mater. 36 (2026) e14936–e14947, doi:10.1002/adfm.202514936.
[40] A.C. Foucher, H.T. Ngan, T. Shirman, A. Filie, K. Duanmu, M. Aizenberg, R.J. Madix, C.M. Friend, J. Aizenberg, P. Sautet, E.A. Stach, Influence of Pd concentration in Au-Pd nanoparticles for the hydrogenation of alkynes, ACS Appl. Nano Mater. 6 (2023) 22927–22938, doi:10.1021/acsanm.3c04278.
[41] Q.S. Wu, G.G. Zhang, Y.Y. Wang, Y.Q. Jiao, Y.Y. Ma, Y.Q. Zheng, Seeded growth of gold-based nanoscale homojunctions via controlled etching regrowth and their applications for methanol oxidation reaction, Crystengcomm 25 (2023) 660–670, doi:10.1039/d2ce01573k.
[42] G.G. Zhang, Y.Y. Wang, Y.Y. Ma, Y.Q. Zheng, H.F. Zhang, M.Y. Tang, Y.Q. Dai, Ultrathin samarium-doped palladium nanocrystals with exotic shapes for efficient electrocatalytic ethanol oxidation, Catal. Today 409 (2023) 63–70, doi:10.1016/j.cattod.2022.03.024.
[43] X.J. Wu, Y.Y. Sun, Y.L. Zeng, X.Y. Li, Mechanistic insights into oxazolone synthesis by bimetallic Au-Pd-catalyzed catalysis and catalyst design: DFT investigations, J. Org. Chem. 88 (2023) 10693–10700, doi:10.1021/acs.joc.3c00751.
[44] C.S. Wu, H. Li, H.P. He, Y.H. Song, C.X. Bi, W. Du, H.B. Xia, Compressive strain in core-shell Au-Pd nanoparticles introduced by lateral confinement of deformation twinnings to enhance the oxidation reduction reaction performance, ACS Appl. Mater. Interfaces 11 (2019) 46902–46911, doi:10.1021/acsami.9b16994.
[45] M. Miyazaki, S. Furukawa, T. Komatsu, Correlation between activation energy and the electronic state of Pd-based bimetallic catalysts for H_2-D_2 equilibration obtained by XPS and DFT calculations, Bull. Chem. Soc. Jpn. 93 (2020) 1020–1025, doi:10.1246/bcsj.20200085.
[46] J.R. Kitchin, J.K. Norskov, M.A. Barteau, J.G. Chen, Modification of the surface electronic and chemical properties of Pt(111) by subsurface 3d transition metals, J. Chem. Phys. 120 (2004) 10240–10246, doi:10.1063/1.1737365.
[47] S.K. Das, B. Mohanty, S.C. Sahu, T.J. Sruthi, B. Chakraborty, S. Basu, B.K. Jena, The experimental and theoretical insights on the interaction of AuPd bimetallic nanoentities on graphene: A study on electrocatalytic activity towards oxygen reduction reaction, Electrochim. Acta 356 (2020) 136820–136828, doi:10.1016/j.electacta.2020.136820.
[48] Z.H. Jin, J.M. Ji, Q.G. He, X.K. Yang, Y.J. Zhang, M.L. Xu, The enhanced electrocatalytic performance of Au@Pd nanoparticles self-assembled on fluorine-modified multi-walled carbon nanotubes for methanol oxidation, Catal. Lett. 148 (2018) 3281–3291, doi:10.1007/s10562-018-2511-4.
[49] M.M. Zhang, X. Zhang, M. Lv, X.R. Yue, Z.K. Zheng, H.B. Xia, Ethanol oxidation via 12-electron pathway on spiky Au@AuPd nanoparticles assisted by near-infrared light, Small 19 (2023) 2205781, doi:10.1002/smll.202205781.
[50] C. Wu, H. Li, H. He, Y. Song, C. Bi, W. Du, H. Xia, Compressive strain in core-shell Au-Pd nanoparticles introduced by lateral confinement of deformation twinnings to enhance the oxidation reduction reaction performance, ACS Appl. Mater. Interfaces 11 (2019) 46902–46911, doi:10.1021/acsami.9b16994.
[51] B. Hammer, J.K. Norskov, Why gold is the noblest of all the metals, Nature 376 (1995) 238–240, doi:10.1038/376238a0.
[52] Z.L. Fan, Z.B. Lu, S.H. Zhan, T. Zhang, Sabatier phenomenon in chemoselective gas-sensing reactions induced by Ag cluster coordination, J. Colloid Interface Sci. 674 (2024) 993–1003, doi:10.1016/j.jcis.2024.06.245.
[53] Y.H. Ma, S.C. Li, X.Q. Yang, Y.W. Li, R.Y. Bian, A. Hameed, X. Chen, X.W. Li, S.J. Liu, K. Wang, P. Chen, P. Li, Entropy-mediated ultrafine PdSnPtAgBi nanoparticles as a high-performance electrocatalyst with enhanced CO tolerance for alcohol oxidation, J. Colloid Interface Sci. 705 (2026) 139515–139524, doi:10.1016/j.jcis.2025.139515.
[54] S.Y. Xu, L.P. Zhang, Y.Y. Zhang, Y.K. Peng, Z.X. Zang, Y.F. Cao, T.F. Li, L.F. Zhang, C.L. Yan, T. Qian, Alleviating O-intermediates adsorption strength over PdRhCu

ternary metallene via ligand effect for enhanced oxygen reduction in practical PEMFCs, J. Phys. Chem. Lett. 16 (2025) 1899–1908, doi:10.1021/acs.jpclett.4c03536.
[55] X. Zhou, Y. Ma, Y. Ge, S. Zhu, Y. Cui, B. Chen, L. Liao, Q. Yun, Z. He, H. Long, L. Li, B. Huang, Q. Luo, L. Zhai, X. Wang, L. Bai, G. Wang, Z. Guan, Y. Chen, C.S. Lee, J. Wang, C. Ling, M. Shao, Z. Fan, H. Zhang, Preparation of Au@Pd core-shell nanorods with fcc-2H-fcc heterophase for highly efficient electrocatalytic alcohol oxidation, J. Am. Chem. Soc. 144 (2022) 547–555, doi:10.1021/jacs.1c11313.
[56] N. Tian, Z.Y. Zhou, S.G. Sun, Y. Ding, Z.L. Wang, Synthesis of tetrahexahedral platinum nanocrystals with high-index facets and high electro-oxidation activity, Science 316 (2007) 732–735, doi:10.1126/science.1140484.
[57] M. Mamatkulov, V.P. Zhdanov, Ostwald ripening of supported metal nanoparticles: Role of dimers and other general trends, Chem. Eng. Sci. 308 (2025), doi:10.1016/j.ces.2025.121373.
[58] W.P. Xiao, M.A.L. Cordeiro, M.X. Gong, L.L. Han, J. Wang, C. Bian, J. Zhu, H.L. Xin, D.L. Wang, Optimizing the ORR activity of Pd based nanocatalysts by tuning their strain and particle size, J. Mater. Chem. A 5 (2017) 9867–9872, doi:10.1039/c7ta02479g.
[59] Y. Ning, J.P. Tang, S.Q. Wang, S. Chen, C. Chen, X.F. Wu, H.Q. Fan, Y.Y. Ma, X.Z. Ma, H.Q. Xie, D.H. Lin, S.G. Sun, Enhanced performance of phosphorus-doped graphene-supported Pd electrocatalysts for ethanol oxidation, Int. J. Hydrogen Energy 126 (2025) 326–335, doi:10.1016/j.ijhydene.2025.04.138.
[60] F.Y. Ding, K. Xiao, P.L. Li, J.F. Song, Y. Shi, G. Jiang, L.S. Zhou, Theoretical insights into electronic structures and durability of single-atom Pd/TiN catalysts, Int. J. Hydrogen Energy 48 (2023) 8954–8964, doi:10.1016/j.ijhydene.2022.12.088.
[61] N. Goswami, K.T. Chen, X.J. Wang, J.S. Spendelow, R.L. Borup, P.P. Mukherjee, Mechanistic understanding of thermodynamic metastability of core-shell catalysts in the polymer electrolyte fuel cell catalyst layer durability, Chem. Eng. J. 484 (2024) 149672–149678, doi:10.1016/j.cej.2024.149672.